Optics Communications 560 (2024) 130463

Contents lists available at ScienceDirect

Optics Communications

journal homepage: www.elsevier.com/locate/optcom

Interactive simulation and visualization of point spread functions in single molecule imaging

Magdalena C. Schneider [a,b,*], Fabian Hinterer [c], Alexander Jesacher [d], Gerhard J. Schütz [b]

[a] HHMI Janelia Research Campus, 19700 Helix Drive, Ashburn, 20147, VA, USA
[b] TU Wien, Institute of Applied Physics, Lehargasse 6, Vienna, 1060, Austria
[c] JKU Linz, Altenbergerstraße 69, Linz, 4040, Austria
[d] Medical University of Innsbruck, Müllerstraße 44, Innsbruck, 6020, Austria

ARTICLE INFO

Dataset link: https://github.com/schneidermc/psf-simulation-app

Keywords:
Point spread function
Single molecule localization microscopy
Simulation
Visualization
MATLAB app
Fluorescence

ABSTRACT

The point spread function (PSF) is fundamental to any type of microscopy, most importantly so for single-molecule localization techniques, where the exact PSF shape is crucial for precise molecule localization at the nanoscale. Optical aberrations and fixed fluorophore dipoles often result in non-isotropic and distorted PSFs, impairing and biasing conventional fitting approaches. Further, PSF shapes are deliberately modified in PSF engineering approaches for providing improved sensitivity, e.g., for 3D localization or determination of dipole orientation. As this can lead to highly complex PSF shapes, a tool for visualizing expected PSFs would facilitate the interpretation of obtained data and the design of experimental approaches. To this end, we introduce a comprehensive and accessible computer application that allows for the simulation of realistic PSFs based on the full vectorial PSF model. Our tool incorporates a wide range of microscope and fluorophore parameters, including orientationally constrained fluorophores, as well as custom aberrations, transmission and phase masks, thus enabling an accurate representation of various imaging conditions. An additional feature is the simulation of crowded molecular environments with overlapping PSFs. Further, our app directly provides the Cramér–Rao bound for assessing the best achievable localization precision under given conditions. Finally, our software allows for the fitting of custom aberrations directly from experimental data, as well as the generation of a large dataset with randomized simulation parameters, effectively bridging the gap between simulated and experimental scenarios, and enhancing experimental design and result validation.

1. Introduction

Single-molecule localization microscopy (SMLM) techniques offer a powerful approach to discern molecular structure and dynamics of biological samples below the diffraction limit [1]. The overall idea is to virtually dilute single molecule signals in time, e.g., by stochastic switching of fluorophores between a bright and a dark state [2,3], by transient binding of fluorescent ligands [4,5], or by massive underlabeling in single molecule tracking [6]. All these methods yield image stacks with very low densities of single molecule signals per frame, which ideally show no overlap. From such images it is possible to estimate the emitter positions to a precision that is mainly limited by the signal to noise ratio of the single molecule images [7].

Crucially, the reliability of the final superresolution images or acquired tracking data critically depends on the quality of the positions obtained from the fitting procedure. In the simplest case, single molecule signals are fitted using a Gaussian function [8]. For this, it is assumed that a fluorophore's emission yields an isotropic point spread function (PSF). However, various factors such as microscope aberrations and fluorophore characteristics alter the shape of the PSF. The mismatch of the fitted simple model of a Gaussian function and the intricate shape of the true PSF may well lead to biases in the estimated positions of up to tens of nanometers, thus highly distorting the obtained results [9]. Hence, it is vital to incorporate a realistic model in the fitting procedure [10–12]. For this purpose, modified Gaussian models [13] or other scalar models, e.g., based on cubic splines [14–17] or Hermite polynomials [18] have been proposed and offer increased accuracy while still retaining the advantages of a scalar model. Vectorial models are preferred when a more accurate representation of the PSF is required, in particular when diffraction and polarization effects are relevant [19–22]. In practice, fluorophores are dipole emitters, and their rotation is often restricted by steric hindrances [23]. Recently, researchers became interested in performing SMLM under cryogenic temperatures [24,25]. Under these conditions, the dipole orientation

* Corresponding author at: HHMI Janelia Research Campus, 19700 Helix Drive, Ashburn, 20147, VA, USA.
E-mail address: schneiderm2@janelia.hhmi.org (M.C. Schneider).

https://doi.org/10.1016/j.optcom.2024.130463
Received 30 November 2023; Received in revised form 31 January 2024; Accepted 10 March 2024
Available online 12 March 2024

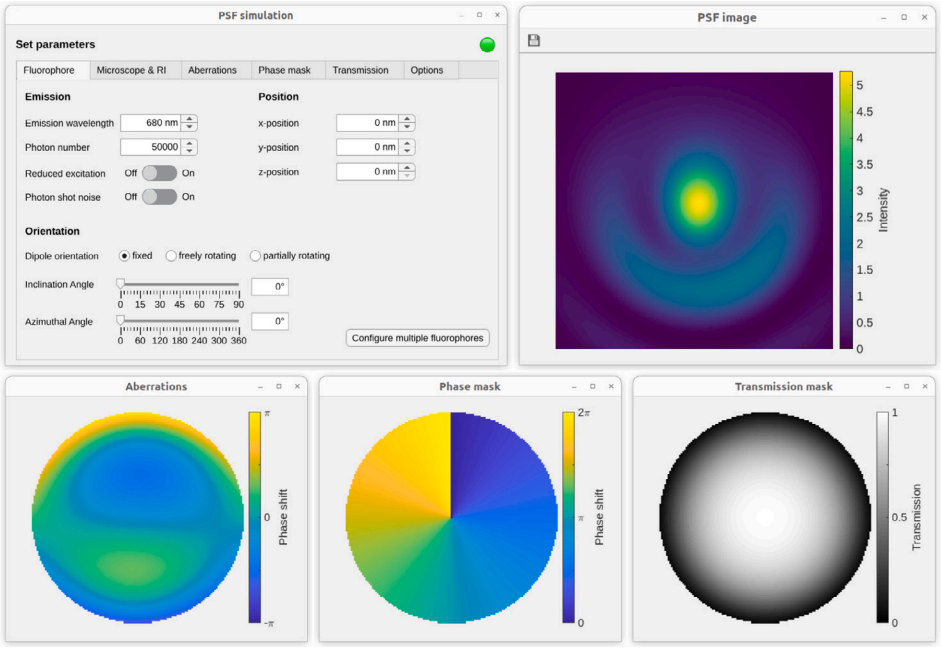

Fig. 1. Overview of app windows. The main app window (top left) comprises several tabs and allows to set all simulation parameters and visualization options. The PSF is visualized in a separate window (top right). The bottom row shows the aberration (left), the applied phase mask (middle) and transmission mask (right).

of a fluorophore is fixed, which leads to generally anisotropic emission patterns and altered PSFs [26]. In addition, to account for the aberrations present in a specific setup, it is necessary to characterize its specific aberrations via phase retrieval. Various algorithms have been proposed for calibration of the microscope aberrations [12,27].

A wide range of SMLM software packages have been developed previously that incorporate PSF simulation [28–30]. Most of these packages, however, focus on entire SMLM datasets, including the simulation of SMLM recordings and data post-processing (e.g., localization). In order to enable easier access to an exact PSF simulation and visualization, we have developed a comprehensive and accessible computer application that allows for interactive simulation and visualization of realistic PSFs under a wide range of microscope and fluorophore parameters, enabling an accurate representation of various imaging conditions. For our application, we implement the full vectorial PSF model [19–21]. In contrast to previous tools for precise PSF calculation [31], we allow to specifically simulate fixed fluorophore dipoles or partial rotation. In addition, we ensured an intuitive user interface.

The best precision that can be achieved in localization techniques depends on the signal to noise ratio, the PSF shape, and the chosen fitting procedure. Ultimately, the localization precision is limited by the Cramér–Rao bound (CRB) [32], which is a theoretical limit for the precision any unbiased estimator can possibly achieve under the given conditions. Notably, the CRB depends on the shape of the PSF. This fact can be taken advantage of by shaping the PSF via manipulations in the back focal plane, often referred to as PSF engineering [1,33]. First, this allows to shape the PSF in a way to achieve best lateral position estimate. Second, this breaks the ground for estimating not only lateral position, but also encoding additional parameters including axial position and dipole orientation in the PSF [23]. To easily assess the effect of different PSF engineering approaches, we included a feature for adding manipulations of the emitted light in the back focal plane in our app. Eventually, we provide the option to directly determine the CRB for any given PSF shape.

In practice, the shape of the PSF is often affected and degraded by various types of aberrations, for example imperfections of the optical setup such as coma, spherical aberrations and astigmatism. These aberrations negatively affect the fitting procedure and lead to decreased quality of the position estimates and all other estimated parameters. In our app, arbitrary aberrations can be easily included using Zernike coefficients. Moreover, we provide an extended feature that allows for fitting a specific microscope's aberrations from data recorded from a calibration sample. The obtained coefficients can be directly loaded back into the PSF simulation app, yielding simulation results tailored to the user's setup.

As additional feature, we implemented the option to simulate multiple fluorophores in the same region of interest. Overlapping PSFs often occur in cryoSMLM applications, as switching of fluorophores between bright and dark states is decelerated under these conditions [25,34]. In addition, overlapping PSFs occur in step-wise photobleaching methods [35], where the signals of multiple fluorophores initially overlap, complicating the localization procedure.

Our application allows to visualize and examine the single fluorophore images, as they would be obtained for specific conditions. It further allows to export the obtained images for further analysis, as well as generating a large dataset of simulated images with randomized parameters. The generated data can be used, e.g., to provide ground truth information for more advanced fitting procedures. The features for import and export of data facilitate a streamlined and accurate approach for the assessment of PSFs under various conditions and PSF engineering approaches.

2. Features

Our application is structured into several subwindows (Fig. 1). The main window allows to set all simulation parameters and visualization options. Fig. 2 shows a schematic overview of the implemented setup and all parameters that can be varied. We simulate the emission of a fluorophore as a dipole emitter and its PSF as observed in a conventional wide-field microscope setup [21]. Here, we will present a short overview of the most important features and illustrative examples of obtained PSFs. For an exhaustive documentation detailing all parameter settings and screenshots of all tabs and subwindows of the app we refer to the app manual in the Supplementary Material.

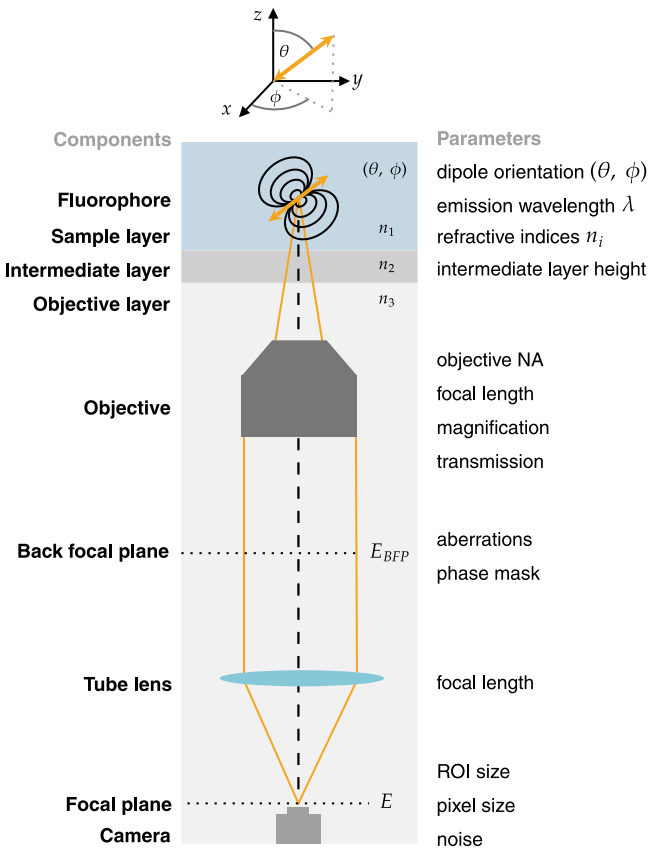

Fig. 2. Schematic of implemented microscope setup. On the left, the components of the microscope are listed; on the right, all the parameters that can be varied in the simulations. E_{BFP} and E are the electric fields in the back focal plane of the objective and in the focal plane of the tube lens, respectively. The path of the ray is simplified and intended to show the infinity space between the objective and the tube lens where phase manipulations can be easily modeled. The inclination angle θ and azimuthal angle ϕ defining the dipole orientation are indicated in the coordinate system on top.

2.1. Fluorophore and microscope parameters

First, the app allows to configure the sample and microscope. The sample is assumed to be a fluorophore, modeled as dipole emitter [21]. We assume that the emitter is embedded in a sample medium (e.g., water), followed by an optional intermediate layer (e.g., a transparent coating) and an objective layer (e.g., immersion oil). The refractive indices of each layer can be specified by the user.

The fluorophore parameters that can be set include the emission wavelength, its lateral and axial position, and the number of observed photons. Further, the fluorophore can be assumed to be either freely rotating, yielding an isotropic PSF, partially rotating, or fixed (Fig. 3a). In the latter case, the dipole orientation of the fluorophore can be specified via its inclination angle θ and azimuthal angle ϕ. For partial rotation, the dipole orientation indicates the center orientation; an additional parameter allows to set the rotational freedom of the fluorophore (see Methods, Section 4.1). In addition, the app allows to account for reduced excitation due to dipole inclination by automatically reducing the number of observed photons. For simplicity, the excitation dipole is assumed to be aligned with the emission dipole here. Further, the actual number of photons in the pixels of the image can be subjected to photon shot noise.

The configurable parameters for the microscope include settings of the tube lens (focal length) and objective (numerical aperture, magnification, focal length). The focus position of the objective is set to the interface between the objective layer and the intermediate layer (or the sample layer in the absence of an intermediate layer), see Fig. 2. The focus position can be adjusted in the simulation by changing the defocus value. A negative (positive) defocus value corresponds to the objective moving closer to (away from) the sample. The effect of the NA and defocusing is shown in (Fig. 3bd).

For the camera, the pixel size can be specified either by setting the physical camera pixel size or the pixel size in object space. Further, background noise can be added to the image (Fig. 3c). The background noise is assumed to follow a Poisson distribution; the parameter for the background noise specifies its standard deviation.

2.2. Multiple fluorophores

Ideally, the signals of active emitters in SMLM are well separated. However, this might not always be the case, in particular for high-density SMLM [36] and stepwise photobleaching methods [35], where the PSFs of several fluorophores may overlap. In addition to single emitters, we allow to configure multiple fluorophores with different positions (lateral and axial) and dipole orientations in the same image. The resulting PSF is the superposition of all individual PSFs and can show a distinctively different shape than the individual PSFs as shown in Fig. 4.

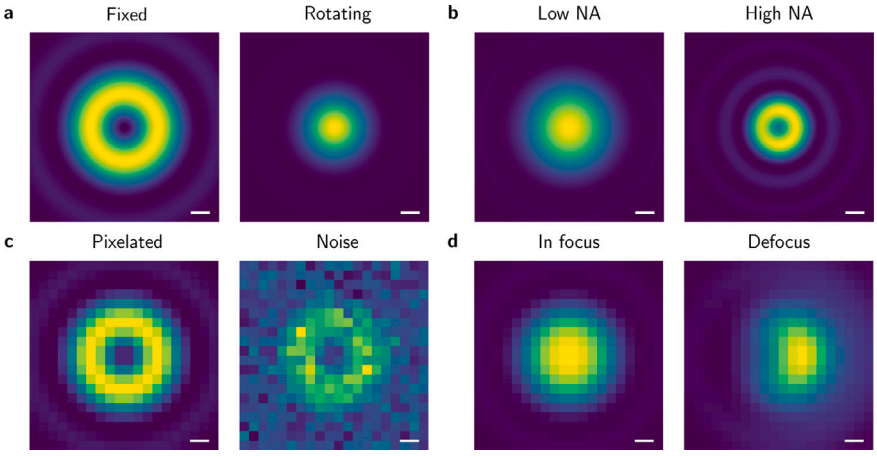

Fig. 3. Fluorophore and microscope parameters. **(a)** Fluorophore with a fixed dipole orientation of $(\theta, \phi) = (0, 0)$ (left) and freely rotating fluorophore (right). **(b)** PSFs shown for a fluorophore with dipole orientation of $(\theta, \phi) = (\frac{\pi}{8}, 0)$ for low and high objective numerical aperture (NA) with NA = 0.7 (left) and NA = 1.2 (right). **(c)** Focal plane pixel size (in object space) of 100 nm without noise (left) and with Poissonian background noise (right). Dipole orientation: $(\theta, \phi) = (0, 0)$. **(d)** PSF in focus (left) and PSF with an objective defocus of 1 µm (right). Dipole orientation: $(\theta, \phi) = (\frac{\pi}{10}, 0)$. Scale bars: 200 nm.

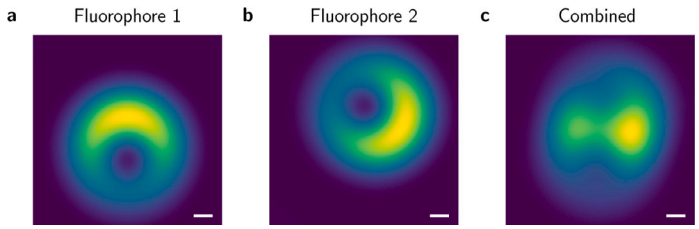

Fig. 4. Multiple fluorophores. Panel **(a)** and **(b)** show individual emitters with different dipole orientations and positions. Fluorophore 1: $(\theta, \phi) = (\frac{\pi}{4}, 0)$, $(x, y, z) = (0, -200, 0)$. Fluorophore 2: $(\theta, \phi) = (\frac{\pi}{4}, \frac{2\pi}{3})$, $(x, y, z) = (100, 200, 0)$. Positions coordinates given in nm. **(c)** Resulting additive PSF. Scale bars: 200 nm.

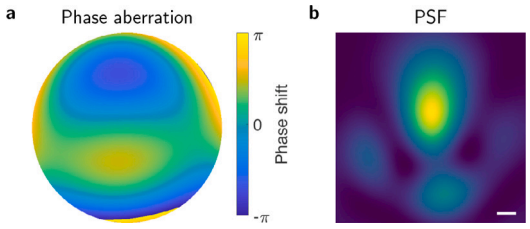

Fig. 5. Aberrations. **(a)** Aberration modeled by phase shift in the back focal plane. **(b)** Resulting aberrated PSF. Scale bar: 200 nm.

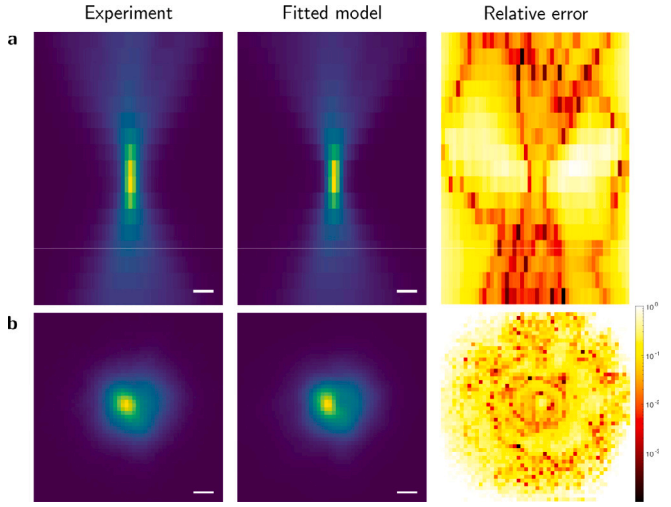

Fig. 6. Phase retrieval. The left column shows the experimental input data, the middle column the calculated model after fitting the aberrations, and the right column the relative error of the model fit in a log-scale. Note that the experimental data is affected by noise, which may lead to high relative errors where the PSF intensity is low. Projections of the PSF onto the xz-plane are shown in **(a)**. Panel **(b)** shows a 2D xy-view of the PSF at the defocus position indicated in panel **(a)** by the white vertical line. Scale bars: 500 nm.

2.3. Aberrations, transmission and phase retrieval

Up to now, we have assumed an ideal PSF only affected by noise. However, imperfections in the optical path or inhomogeneous refractive indices in the sample can lead to aberrated PSF shapes [37]. We allow to include such aberrations in the simulation by introducing a phase shift in the back focal plane that is expanded into a linear combination of Zernike polynomials (see Eq. (6)). The most common aberrations, including spherical aberrations, astigmatism and coma can be directly selected and their coefficients adjusted. Alternatively, an arbitrary set of Zernike modes and corresponding coefficients can be specified. Fig. 5 shows an illustrative example how aberrations can affect the PSF shape.

In addition, the PSF shape can be affected by apodization, i.e., non-homogeneous transmission of the emitted light through the objective. In particular, towards the outer rim of the objective, light transmission is reduced [38]. In order to model this attenuation, the app allows to load a custom transmission mask.

As an additional feature, we provide a subroutine that allows for retrieving the aberrations and transmission of a specific setup from experimental data. For this, a stack of images at various defocus positions from a calibration sample (a fluorescent bead) is required. For details on the recording of the calibration data see 4.5. An illustrative example of experimental data and the fitted model is shown in Fig. 6.

2.4. Phase masks

In contrast to undesired aberrations, phase manipulations can be used deliberately in PSF engineering approaches. Here, phase shifts are exploited for shaping the PSF in a way that allows to encode more information. For example, the double helix PSF has been used to allow for determination of the axial position [39], and a vortex phase mask has been shown to allow for retrieving information about the lateral and axial position, as well as the emitter's dipole orientation [23]. Any such phase manipulation can be introduced by adding an additional phase factor in the back focal plane (see Eq. (5)). Our app offers the feature to select from a variety of commonly used phase masks, including the vortex, double helix, and pyramid phase masks. In addition, a custom phase mask can be loaded. Further, the selected phase masks can be altered by cutting out an inner disk or rotation of the phase mask. A selection of phase masks and their influence on the PSF shape is given in Fig. 7.

2.5. Visualization options

Our app allows to visualize the calculated PSF for a set of given parameters in several ways (see Fig. 8). The default visualization option is a 2D lateral view of the PSF. In addition to the full PSF, the emission can be split into x- and y-polarization channels that can be viewed separately. Further, a full 3D model of the PSF can be calculated. For visualization, we show an xz-projection along with an isosurface plot. The value of the isosurface can be adjusted to show various isosurfaces of the 3D PSF.

The visualization of the plots can be adjusted in several ways as depicted in Fig. 9. First, the simulated region of interest can be specified by setting either the side length of the desired region of interest or the number of pixels per lateral axis (panel a). Second, in case of high background noise, adjusting the contrast of the image may help to better discern the PSF shape (panel b). Third, the colormap of the images can be set by selecting from a few options including the viridis, parula, hot and gray colormaps (panel c).

2.6. Import and export options

As noted in the previous subsections, our application allows to import custom data for aberrations, phase masks and transmission. In the subwindow for fitting of the PSF model to experimental data, the fitting results (including aberrations and transmission) can be exported. The saved aberrations and transmission can then be imported into the main window via the aberration and transmission tabs. This allows to

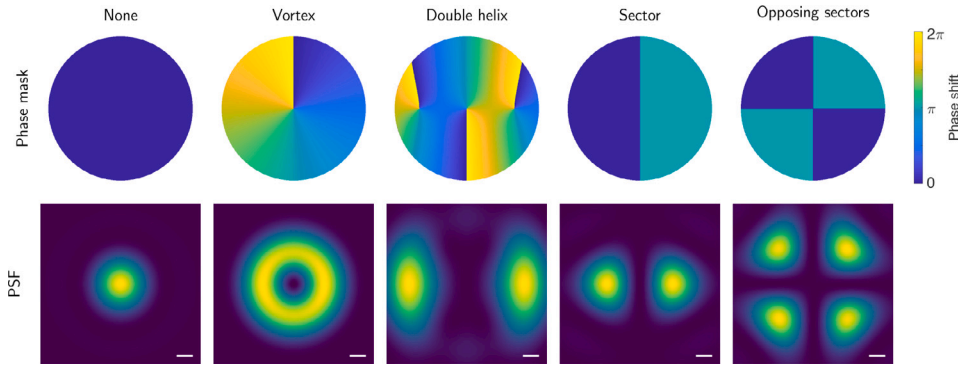

Fig. 7. Phase masks. The top row shows the phase shift introduced by various phase masks and the bottom row the resulting PSF shape.

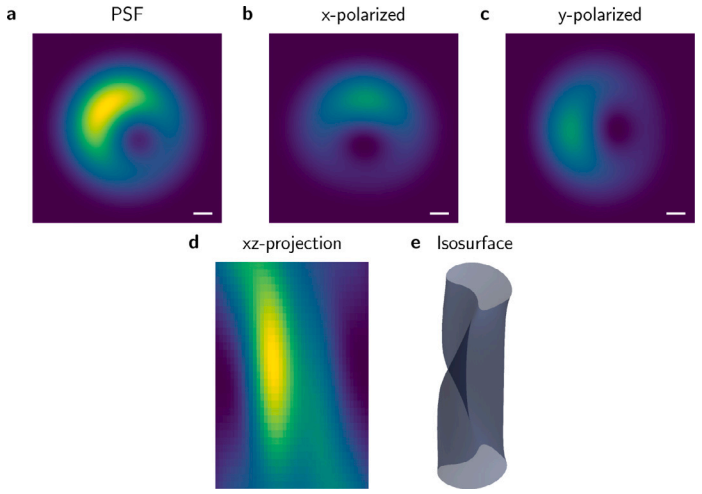

Fig. 8. PSF visualization. The top row shows visualization options in 2D, including the 2D PSF **(a)** and the split of the emission into polarized channels, **(b)** and **(c)**. The bottom row shows visualization options for the 3D PSF. **(d)** xz-projection of the 3D PSF. **(e)** Isosurface of 3D PSF. Scale bars: 200 nm.

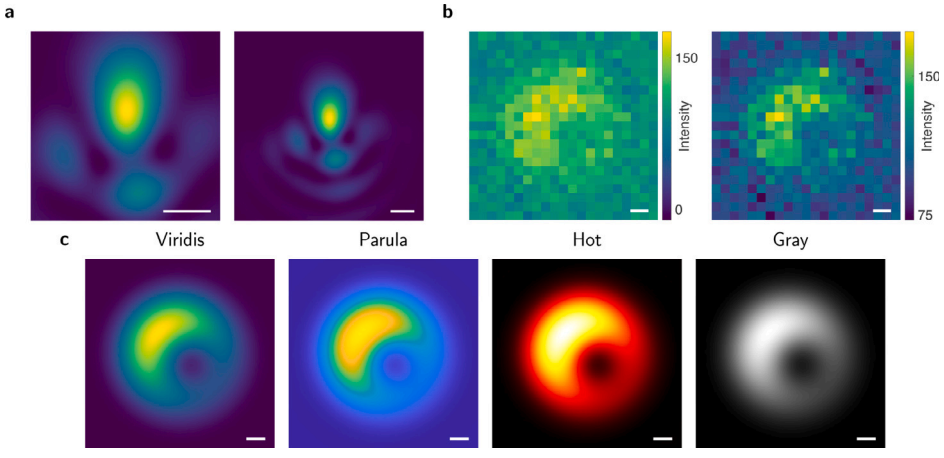

Fig. 9. Visualization adjustments. **(a)** Size of region of interest. **(b)** Image contrast. Left: low contrast, right: high contrast. **(c)** Colormap options. Scale bars: 500 nm (panel a), 200 nm (panels b–c).

incorporate the fit results directly into the simulated model. The calculated simulation data for 2D and 3D PSFs can be exported under the tab *Options* for further processing or benchmarking of fitting algorithms.

2.7. Generation of randomized dataset

As additional feature, our app allows to generate a large dataset of PSF images with randomized simulation parameters in the tab *Options*. The user can choose which parameters are randomized and set ranges for each randomized parameter. The used parameters and corresponding calculated PSFs are exported, and provide ground truth for testing and devising PSF fitting approaches.

2.8. Cramér–Rao bound

Finally, the theoretically achievable localization precision for lateral and axial position can be directly calculated in our app under the tab *Options*. We calculate the CRB as the diagonal elements of the inverse Fisher information matrix (see Eq. (7)). The CRB is affected by the shape of the PSF, the number of observed photons and the background noise. Note that in some cases the PSF does not provide enough information to estimate a particular parameter. For example, the axial position of a molecule that is in focus cannot be accurately estimated from an isotropic PSF in the absence of PSF engineering. In this case, numerical errors lead to unstable values of the CRB. Thus, we do not provide an exact value for the CRB if the calculated number is greater than 1000 nm, i.e., much greater than the diffraction limit of around 200 nm.

3. Conclusion and outlook

We have presented an easy-to-use MATLAB application that enables the simulation of point spread functions as they appear in SMLM applications. Reflecting the variability in experimental setups, the application offers a wide range of customizable parameters. This allows to tailor the simulation to specific microscope setups, ensuring that the simulated data closely aligns with the experimental reality. The key features of the application include:

- simulation of fixed, partially and freely rotating dipole emitters
- simulation of aberrations modeled by Zernike polynomials in the objective pupil
- addition of optical elements such as phase masks and polarizers in the emission path
- retrieval of Zernike aberrations from an experimentally recorded PSF stack
- calculation of the Cramér Rao Bound to assess the theoretically achievable localization precision under specific conditions
- flexible visualization options
- generation of a large dataset of PSF images with randomized simulation parameters.

The results can be exported in various formats, allowing users to easily generate simulated data for an array of purposes. Most of the parameters can be adjusted via sliders or numerical input fields with a near real-time calculation and visualization of the PSF. While we strived to offer computational efficiency for this first release of our app, a further speed up of calculations, in particular for 3D PSFs and small pixel size, can be achieved in future releases by leveraging GPU capabilities. The features of this app and its interactivity allows users to observe the effect of specific parameters on the shape of the PSF, which, combined with the Cramér–Rao bound may assist, e.g., in designing novel PSF engineering approaches.

4. Mathematical model

We start by stating the PSF model for a fixed dipole emitter situated on the optical axis in an aberration-free optical system as illustrated in Fig. 2. We assume that the emitter is embedded in a sample medium, followed by an intermediate layer and an objective layer. The interfaces are assumed to be planes orthogonal to the optical axis.

The angles (θ, ϕ) represent the inclination and azimuth angles characterizing the dipole orientation. We denote by λ the emission wavelength in vacuum and by $\vec{x}_b \in \mathbb{R}^2$ and $\vec{x}_f \in \mathbb{R}^2$ coordinates in the back focal plane and image plane, respectively.

The dipole emission pattern, polarization-dependent refraction and reflection between the different layers of medium according to Fresnel equations, and subsequent passage through the infinity-corrected objective are comprehensively described in [21]. The starting point of our model is the electric field vector $E_{\mathrm{BFP}} = E_{\mathrm{BFP}}(\vec{x}_b; \theta, \phi)$, expressed in Cartesian coordinates. This field in the back focal plane is defined by [21, Eq. (18)].

A tube lens with focal length f is positioned between the objective and the camera to produce the image. The passage of the unaberrated field through this tube lens is modeled by the Fourier transform,

$$E(\vec{x}_f) = \mathcal{F}(E_{\mathrm{BFP}})(\vec{x}_f) = \frac{1}{i\lambda f} e^{\frac{2i\pi}{\lambda f}\|\vec{x}_f\|} \int E_{\mathrm{BFP}}(\vec{x}_b) e^{-\frac{2\pi i}{\lambda f}\vec{x}_b \cdot \vec{x}_f} d\vec{x}_b \,. \tag{1}$$

Integration is performed over the circular pupil area. The intensity distribution in the focal plane of the tube lens is given by the absolute value of the electric field,

$$I(\vec{x}_f) = |E(\vec{x}_f)|^2. \tag{2}$$

The coordinate system in the back focal plane can in principle be chosen arbitrarily. If one uses emission polarizers, the directions of $\vec{x}_b$ are chosen to lie along the orthogonal directions of those polarizers. Then the field resulting from a linear polarizer oriented to transmit x-polarization (y-polarization) only is given by the first (second) component of $E(\vec{x}_f)$ [21].

4.1. Rotational freedom and multiple emitters

The isotropic PSF resulting from a freely rotating emitter is modeled as the superposition of three fluorophores with pairwise orthogonal orientations. The PSF of a partially rotating emitter (I_{partial}) is based on a weighted sum of the freely rotating dipole PSF (I_{free}) and the fixed dipole PSF (I_{fixed}), following [23,40]:

$$I_{\mathrm{partial}} = \frac{1-g}{3} I_{\mathrm{fixed}} + \frac{g}{3} I_{\mathrm{free}}, \tag{3}$$

where $g \in [0, 1]$ describes the rotational freedom of the dipole. A value of $g = 0$ and 1 corresponds to a fixed or freely rotating dipole, respectively.

The intensity pattern resulting from multiple nearby emitters is calculated as the superposition of the respective individual intensities.

4.2. Discretization, signal and noise

The BFP field E_{BFP} is calculated as implementation of Eqs. (10)-(18) from Ref. [21] on a quadratic grid of $n_{\mathrm{BFP}} \times n_{\mathrm{BFP}}$. The discretization parameter can be adjusted in the *Options* tab; as default, we use $n_{\mathrm{BFP}} = 129$. For the calculation of the Fourier transform in (1), we employ the chirp-Z-transform, which allows for flexibility in the number of discretization points [41].

To simulate the pixelated grid of the camera, we consider the integrated intensity over the kth pixel $\square_k$,

$$I_k = \int_{\square_k} I(\vec{x}_f) d\vec{x}_f \,. \tag{4}$$

We call the amount of supporting points used in each dimension for the calculation of (4) the *oversampling factor*. We set this value to 9, which provides an accurate calculation while maintaining low computational cost [10].

We normalize the pixelated intensity and scale it to the user-set photon count. In the case of a 3D PSF, the normalization factor is

calculated from the in-focus slice. Camera shot noise is modeled via the realization of a Poissonian random variable, with the calculated noise-free PSF as the mean. A constant background may be added before the application of the Poissonian random variable to model the fluorescence emission of a homogeneous background.

4.3. Aberrations, phase mask, transmission and defocus

The infinity-corrected optical system provides a space between the objective and the tube lens, where additional optical components such as phase plates can be placed. Any wavefront deformation in this space, either caused by aberration or deliberate distortion, can be modeled as

$$E(\vec{x}_f) = \mathcal{F}(T e^{\frac{2i\pi}{\lambda}\varphi} E_{\mathrm{BFP}})(\vec{x}_f), \tag{5}$$

where T and ϕ represent attenuation and phase aberration, respectively. We split the phase into two separate parts, $\varphi = \varphi_z + \varphi_r$, where φ_z is a Zernike term and φ_r models the addition of further optical elements, e.g., phase masks in the back focal plane, see Section 2. We expand φ_z into a linear combination of orthonormal Zernike polynomials, i.e.,

$$\varphi_z(\vec{x}_b) = \sum_i w_i Z_i(\vec{x}_b), \tag{6}$$

where Z_i, denotes the ith Zernike polynomial (using Noll's indices [42]) and w_i is the corresponding Zernike coefficient. In particular, we use tip and tilt to model the PSF of an emitter that is laterally displaced from the optical axis. Setting $w_{1,2} = 1\lambda$ produces a lateral shift of $\frac{2}{\mathrm{NA}}\lambda$ in horizontal and vertical direction, respectively. To model the potentially non-uniform transmission of light through the optical system, a transmission mask $T(\vec{x}_b)$ (taking values between 0 and 1) describing the amplitude modulation is multiplied with the field in the back focal plane in (5). For modeling the axial position of the focus (i.e., defocusing of the objective), we include an additional defocus term in the phase by adding a spherical defocus function as described in [43].

4.4. Cramér–Rao bound

We calculate the Cramér Rao Bound (CRB), which is a tool from estimation theory that provides a benchmark for the achievable precision of an estimator [32]. Hence, the CRB can be used for quantitative comparison of PSFs under various conditions regarding their performance to encode the lateral and axial position of fluorophores. The CRB is given by the diagonal elements of the inverse Fisher information matrix of the likelihood function. The likelihood function can be constructed from the forward model (4) and an appropriate noise model. As noise model we choose Poissonian noise, which is a good approximation for camera shot noise. Following [44], we can then calculate the Fisher information as

$$\mathcal{I}_{ij} = \sum_k \frac{\partial I_k}{\partial \xi_i} \frac{\partial I_k}{\partial \xi_j} \frac{1}{I_k}, \tag{7}$$

where the summation is over the pixels of the image. The parameter vector ξ denotes the parameters that one wishes to estimate, which is typically just the lateral position. However, they could also include axial position or orientation. The Fisher information matrix is always a symmetric matrix with as many rows as the amount of parameters that are estimated.

4.5. Phase retrieval

The PSFs of real microscopes usually differ from the theoretical model. This is in one part explained by the design of the optical elements, in particular the objective lens. Although a modern microscope objective consists of many individual lenses, truly isoplanatic imaging performance cannot be obtained and significant amounts of astigmatism and coma appear at increasing distance from the optical axis. Other effects are known to introduce spherical aberrations, predominantly a refractive index mismatch between the sample buffer solution and objective immersion medium, but also too high or low environmental temperatures or age-related refractive index changes of the immersion oil. Even when these aberrations are small, they can cause systematic errors in the molecule position estimates on the order of several tens to hundreds of nanometers.

In order to avoid these errors, we include phase aberrations in the model via the Zernike term φ_r. To account for the decreasing objective transmission at higher numerical apertures, we also include a radially symmetric attenuation (apodization) mask in the pupil, whose radial profile is modeled by a 6th degree polynomial. For reasons of symmetry, the odd coefficients are set to zero. The necessary Zernike phase coefficients and polynomial apodization coefficients are estimated by a phase retrieval algorithm [45] which operates on an experimental 3D image (*z-stack*) acquired from a single small fluorescent bead. The algorithm finds coefficients that minimize the squared L2-Norm of a vectorial error metric ϵ, which is defined as

$$\epsilon_k = \frac{|E_k^\gamma|}{\sum_k |E_k^\gamma|} - \frac{|S_k^\gamma|}{\sum_k |S_k^\gamma|}. \tag{8}$$

Here, E and S represent the experimentally recorded and simulated three-dimensional bead intensity images and k the voxel index. The quantity γ is a user-definable scalar value between 0 and 1 that influences the fit performance. Smaller values of γ assign increased weight to voxels of lower intensity, e.g., those in out-of-focus planes. We discovered that a γ value of 0.5 was effective in the tested cases, whereas a value of 1 led to inaccuracies as the algorithm stopped at non-ideal local minima. To account for the bead size we convolve the simulated 3D intensity PSF with a sphere of the bead diameter as described in [46]. Within the optimization loop this step is taken at each iteration before the calculated PSF is compared to the experimental recording.

Appropriate z-stacks should be recorded at a maximum possible signal to noise ratio and contain about 10 widefield images covering an axial range from about -1 to $1\,\mu\mathrm{m}$ around the axial bead position. Ideally, the bead is immersed in a mounting medium with a refractive index higher than the NA of the objective. This avoids the formation of a supercritical angle fluorescence (SAF) zone in the objective pupil, and also avoids complications caused by fluorophores located in different regions within the bead emitting different amounts of SAF. The diameter of the bead should not be larger than 200 nm. For capturing spatially varying aberrations, the bead can be imaged at multiple lateral positions across the field of view (FOV). The retrieved aberrations at the recorded positions can subsequently be used to inform a deep learning model describing a spatially varying PSF [27].

CRediT authorship contribution statement

Magdalena C. Schneider: Writing – original draft, Visualization, Validation, Software, Project administration, Methodology, Investigation, Funding acquisition, Formal analysis, Conceptualization. **Fabian Hinterer:** Writing – original draft, Visualization, Validation, Software, Methodology, Investigation, Formal analysis, Conceptualization. **Alexander Jesacher:** Writing – original draft, Software, Methodology, Investigation, Funding acquisition, Formal analysis, Conceptualization. **Gerhard J. Schütz:** Writing – review & editing, Project administration, Funding acquisition, Conceptualization.

Declaration of competing interest

The authors declare that they have no known competing financial interests or personal relationships that could have appeared to influence the work reported in this paper.

Data availability

Source code, app files and sample data are provided on GitHub: https://github.com/schneidermc/psf-simulation-app.

Acknowledgments

MCS was funded by Howard Hughes Medical Institute, USA, Janelia Research Campus. GJS and AJ were funded by the Austrian Science Fund (FWF): P-36022B. GJS and MCS were funded by the Austrian Science Fund (FWF): F6809-N36. FH was funded by the Austrian Science Fund (FWF): F6805-N36.

This article is subject to HHMI's Open Access to Publications policy. HHMI has previously granted a nonexclusive CC BY 4.0 license to the public and a sublicensable license to HHMI in their research articles. Pursuant to those licenses, the author-accepted manuscript of this article can be made freely available under a CC BY 4.0 license immediately upon publication.

This research was funded in whole or in part by the Austrian Science Fund (FWF) SFB 10.55776/F68 "Tomography Across the Scales", subprojects F6805-N36 and F6809-N36 and 10.55776/P36022 "Live Cell Superresolution Imaging of Protein Conformation". For open access purposes, the authors have applied a CC BY public copyright license to any author-accepted manuscript version arising from this submission.

Appendix A. Supplementary data

The Supplementary material includes a detailed manual of the app and a table with all simulation parameters used for creating the PSF images for the manuscript figures. The app files are provided on GitHub under the following link: https://github.com/schneidermc/psf-simulation-app.

Supplementary material related to this article can be found online at https://doi.org/10.1016/j.optcom.2024.130463.

References

[1] M. Lelek, M.T. Gyparaki, G. Beliu, F. Schueder, J. Griffié, S. Manley, R. Jungmann, M. Sauer, M. Lakadamyali, C. Zimmer, Single-molecule localization microscopy, Nat. Rev. Methods Primers 1 (1) (2021) 39.

[2] M. J. Rust, M. Bates, X. Zhuang, Sub-diffraction-limit imaging by stochastic optical reconstruction microscopy (STORM), Nat. Methods 3 (2006) 793–795, http://dx.doi.org/10.1038/nmeth929.

[3] E. Betzig, G.H. Patterson, R. Sougrat, O.W. Lindwasser, S. Olenych, J.S. Bonifacino, M.W. Davidson, J. Lippincott-Schwartz, H.F. Hess, Imaging intracellular fluorescent proteins at nanometer resolution, Science 313 (5793) (2006) 1642–1645.

[4] A. Sharonov, R.M. Hochstrasser, Wide-field subdiffraction imaging by accumulated binding of diffusing probes, Proc. Natl. Acad. Sci. 103 (50) (2006) 18911–18916.

[5] R. Jungmann, C. Steinhauer, M. Scheible, A. Kuzyk, P. Tinnefeld, F.C. Simmel, Single-molecule kinetics and super-resolution microscopy by fluorescence imaging of transient binding on DNA origami, Nano Lett. 10 (11) (2010) 4756–4761.

[6] S. Wieser, G.J. Schütz, Tracking single molecules in the live cell plasma membrane—Do's and Don't's, Methods 46 (2) (2008) 131–140.

[7] C.S. Smith, N. Joseph, B. Rieger, K.A. Lidke, Fast, single-molecule localization that achieves theoretically minimum uncertainty, Nature Methods 7 (5) (2010) 373–375, http://dx.doi.org/10.1038/nmeth.1449.

[8] B. Huang, W. Wang, M. Bates, X. Zhuang, Three-dimensional super-resolution imaging by stochastic optical reconstruction microscopy, Science 319 (5864) (2008) 810–813, http://dx.doi.org/10.1126/science.1153529.

[9] J. Engelhardt, J. Keller, P. Hoyer, M. Reuss, T. Staudt, S.W. Hell, Molecular orientation affects localization accuracy in superresolution far-field fluorescence microscopy, Nano Lett. 11 (1) (2011) 209–213, http://dx.doi.org/10.1021/nl103472b.

[10] F. Hinterer, M.C. Schneider, S. Hubmer, M. López-Martinez, P. Zelger, A. Jesacher, R. Ramlau, G.J. Schütz, Robust and bias-free localization of individual fixed dipole emitters achieving the Cramér Rao bound for applications in cryo-single molecule localization microscopy, PLoS One 17 (2) (2022) e0263500, http://dx.doi.org/10.1371/journal.pone.0263500.

[11] F. Hinterer, M.C. Schneider, S. Hubmer, M. López-Martínez, R. Ramlau, G.J. Schütz, Localization of fixed dipoles at high precision by accounting for sample drift during illumination, Appl. Phys. Lett. 123 (2) (2023) 023703, http://dx.doi.org/10.1063/5.0137834.

[12] B. Ferdman, E. Nehme, L.E. Weiss, R. Orange, O. Alalouf, Y. Shechtman, VIPR: vectorial implementation of phase retrieval for fast and accurate microscopic pixel-wise pupil estimation, Opt. Express 28 (7) (2020) 10179–10198, http://dx.doi.org/10.1364/OE.388248.

[13] M. Backlund, M. Lew, A. Backer, S. Sahl, G. Grover, A. Agrawal, R. Piestun, W. Moerner, Simultaneous, accurate measurement of the 3D position and orientation of single molecules, Proc. Natl. Acad. Sci. USA 109 (2012) http://dx.doi.org/10.1073/pnas.1216687109.

[14] M. Bates, J. Keller, A. Przybylski, A. Hüper, T. Stephan, P. Ilgen, A. Cereceda, E. D'Este, A. Egner, S. Jakobs, S. Sahl, S. Hell, Optimal precision and accuracy in 4Pi-STORM using dynamic spline PSF models, Nature Methods 19 (2022) 1–10, http://dx.doi.org/10.1038/s41592-022-01465-8.

[15] H.P. Babcock, X. Zhuang, Analyzing single molecule localization microscopy data using cubic splines, Sci. Rep. 7 (1) (2017) 552.

[16] Y. Li, M. Mund, P. Hoess, J. Deschamps, U. Matti, B. Nijmeijer, V.J. Sabinina, J. Ellenberg, I. Schoen, J. Ries, Real-time 3D single-molecule localization using experimental point spread functions, Nat. Methods 15 (5) (2018) 367–369.

[17] Y. Li, E. Buglakova, Y. Zhang, J.V. Thevathasan, J. Bewersdorf, J. Ries, Accurate 4Pi single-molecule localization using an experimental PSF model, Opt. Lett. 45 (13) (2020) 3765–3768.

[18] S. Stallinga, B. Rieger, Position and orientation estimation of fixed dipole emitters using an effective Hermite point spread function model, Opt. Express 20 (6) (2012) 5896–5921, http://dx.doi.org/10.1364/OE.20.005896.

[19] F. Aguet, S. Geissbühler, I. Märki, T. Lasser, M. Unser, Super-resolution orientation estimation and localization of fluorescent dipoles using 3-D steerable filters, Opt. Express 17 (8) (2009) 6829–6848, http://dx.doi.org/10.1364/OE.17.006829.

[20] K. Mortensen, L. Churchman, J. Spudich, H. Flyvbjerg, Optimized localization analysis for single-molecule tracking and super-resolution microscopy, Nat. Methods 7 (2010) 377–381, http://dx.doi.org/10.1038/nmeth.1447.

[21] D. Axelrod, Fluorescence excitation and imaging of single molecules near coated surfaces: A theoretical study, J. Microsc. 247 (2012) 147–160, http://dx.doi.org/10.1111/j.1365-2818.2012.03625.x.

[22] T. Yan, C.J. Richardson, M. Zhang, A. Gahlmann, Computational correction of spatially variant optical aberrations in 3D single-molecule localization microscopy, Opt. Express 27 (9) (2019) 12582–12599, http://dx.doi.org/10.1364/OE.27.012582.

[23] C.N. Hulleman, R.Ø. Thorsen, E. Kim, C. Dekker, S. Stallinga, B. Rieger, Simultaneous orientation and 3D localization microscopy with a vortex point spread function, Nature Commun. 12 (1) (2021) 5934.

[24] S. Weisenburger, D. Boening, B. Schomburg, K. Giller, S. Becker, C. Griesinger, V. Sandoghdar, Cryogenic optical localization provides 3D protein structure data with angstrom resolution, Nature Methods 14 (2) (2017) 141–144, http://dx.doi.org/10.1038/nmeth.4141.

[25] W. Li, S.C. Stein, I. Gregor, J. Enderlein, Ultra-stable and versatile widefield cryo-fluorescence microscope for single-molecule localization with sub-nanometer accuracy, Opt. Express 23 (3) (2015) 3770–3783, http://dx.doi.org/10.1364/OE.23.003770.

[26] J. Enderlein, E. Toprak, P. Selvin, Polarization effect on position accuracy of fluorophore localization, Opt. Express 14 (2006) 8111–8120, http://dx.doi.org/10.1364/OE.14.008111.

[27] S. Fu, W. Shi, T. Luo, Y. He, L. Zhou, J. Yang, Z. Yang, J. Liu, X. Liu, Z. Guo, et al., Field-dependent deep learning enables high-throughput whole-cell 3D super-resolution imaging, Nature Methods 20 (3) (2023) 459–468.

[28] J. Sinkó, R. Kákonyi, E. Rees, D. Metcalf, A.E. Knight, C.F. Kaminski, G. Szabó, M. Erdélyi, TestSTORM: Simulator for optimizing sample labeling and image acquisition in localization based super-resolution microscopy, Biomed. Opt. Express 5 (3) (2014) 778—787, http://dx.doi.org/10.1364/boe.5.000778.

[29] D. Bourgeois, Single molecule imaging simulations with advanced fluorophore photophysics, Commun. Biol. 6 (2023) 53, http://dx.doi.org/10.1038/s42003-023-04432-x.

[30] D. Sage, T.-A. Pham, H. Babcock, T. Lukes, T. Pengo, R. Velmurugan, A. Herbert, A. Agrawal, B. Rieger, et al., Super-resolution fight club: Assessment of 2D and 3D single-molecule localization microscopy software, Nat. Methods (online) 16 (5) (2019) 387–395, http://dx.doi.org/10.1038/s41592-019-0364-4.

[31] H. Kirshner, F. Aguet, D. Sage, M. Unser, 3-D PSF fitting for fluorescence microscopy: implementation and localization application, J. Microsc. 249 (1) (2013) 13–25, http://dx.doi.org/10.1111/j.1365-2818.2012.03675.x.

[32] S.M. Kay, Fundamentals of Statistical Signal Processing: Estimation Theory, Prentice-Hall, Inc., Upper Saddle River, NJ, USA, 1993.

[33] K. Khare, M. Butola, S. Rajora, PSF engineering, in: Fourier Optics and Computational Imaging, Springer International Publishing, Cham, 2023, pp. 249–260, http://dx.doi.org/10.1007/978-3-031-18353-9_17.

[34] C.N. Hulleman, W. Li, I. Gregor, B. Rieger, J. Enderlein, Photon yield enhancement of red fluorophores at cryogenic temperatures, ChemPhysChem 19 (14) (2018) 1774–1780.

[35] M.P. Gordon, T. Ha, P.R. Selvin, Single-molecule high-resolution imaging with photobleaching, Proc. Natl. Acad. Sci. 101 (17) (2004) 6462–6465, http://dx.doi.org/10.1073/pnas.0401638101.

[36] R.J. Marsh, K. Pfisterer, P. Bennett, L.M. Hirvonen, M. Gautel, G.E. Jones, S. Cox, Artifact-free high-density localization microscopy analysis, Nat. Methods 15 (9) (2018) 689–692.

[37] S. Ghosh, C. Preza, Fluorescence microscopy point spread function model accounting for aberrations due to refractive index variability within a specimen, J. Biomed. Opt. 20 (2015) 075003, http://dx.doi.org/10.1117/1.JBO.20.7.075003.

[38] J. Pawley, Handbook of Biological Confocal Microscopy, vol. 236, Springer Science & Business Media, 2006.
[39] S.R.P. Pavani, M.A. Thompson, J.S. Biteen, S.J. Lord, N. Liu, R.J. Twieg, R. Piestun, W.E. Moerner, Three-dimensional, single-molecule fluorescence imaging beyond the diffraction limit by using a double-helix point spread function, Proc. Natl. Acad. Sci. 106 (9) (2009) 2995–2999.
[40] S. Stallinga, Effect of rotational diffusion in an orientational potential well on the point spread function of electric dipole emitters, J. Opt. Soc. Amer. A 32 (2) (2015) 213–223.
[41] R. Tong, R.W. Cox, Rotation of NMR images using the 2D chirp-z transform, Magn. Reson. Med.: Official J. Int. Soc. Magn. Reson. Med. 41 (2) (1999) 253–256.
[42] R.J. Noll, Zernike polynomials and atmospheric turbulence, J. Opt. Soc. Amer. 66 (3) (1976) 207–211, http://dx.doi.org/10.1364/JOSA.66.000207.
[43] A. Jesacher, M.J. Booth, Parallel direct laser writing in three dimensions with spatially dependent aberration correction, Opt. Express 18 (20) (2010) 21090–21099.
[44] J. Chao, E. Sally Ward, R. Ober, Fisher information theory for parameter estimation in single molecule microscopy: Tutorial, J. Opt. Soc. Amer. A 33 (2016) B36, http://dx.doi.org/10.1364/JOSAA.33.000B36.
[45] P. Zelger, K. Kaser, B. Rossboth, L. Velas, G. Schütz, A. Jesacher, Three-dimensional localization microscopy using deep learning, Opt. Express 26 (2018) 33166, http://dx.doi.org/10.1364/OE.26.033166.
[46] B.M. Hanser, M.G. Gustafsson, D. Agard, J.W. Sedat, Phase-retrieved pupil functions in wide-field fluorescence microscopy, J. Microsc. 216 (1) (2004) 32–48.